ADVANCED INTELLIGENT SYSTEMS
Open Access
www.advintellsyst.com

Robotic Conformal Material Extrusion 3D Printing for Appending Structures on Unstructured Surfaces

*Connor David Armstrong, Stuart Macrae Montgomery, Liang Yue, Frédéric Demoly, Kun Zhou, and H. Jerry Qi**

Fabrication of structures in unstructured conditions is a promising area of bolstering the application spaces of additive manufacturing (AM). One emerging application is appending structures on existing ones that may have nonplanar surfaces in unconventional orientations. However, extrusion-based AM techniques are limited to printing on structured, planar environments with a fixed single-nozzle direction. Herein, the authors present a dexterous conformal material extrusion printing method using a six-axis robotic arm capable of constructing complex parts onto highly unstructured surfaces with rough topographies. The manufacturing method employs a custom algorithm that generates layers consisting of 3D spatial coordinates of print path as well as the extrusion nozzle oriented in the normal direction of the substrate, thereby enabling conformal motion of the extrusion nozzle to the unstructured surface. The capabilities of the surface-informed robotic conformal 3D printing method to fabricate structures on surfaces with a variety of topographies in unconventional orientations are demonstrated. Finally, via addition of deposited conductive paths, a high-strength, functional reinforcement capable of in situ deformation monitoring is appended. This work has the potential for reconstructing, repairing, and reinforcing existing structures in human-limited or inaccessible spaces. Integration of functional elements can also enable in situ sensing, monitoring, and self-diagnosis.

1. Introduction

Extrusion-based additive manufacturing (AM) such as direct ink writing (DIW) and fused filament fabrication (FFF) are popular choices for hobby, research, and commercial operations due to their low cost, simple architecture, and breadth of material feedstocks. Recently, researchers have broadened potential applications of extrusion-based AM by modifying printer hardware, layer structure, control schemes, and even software to accommodate new materials, facilitate fabrication of functional structures, and deposit material in nonplanar environments.[1–6] Moreover, researchers have also utilized DIW material versatility to develop structures with a myriad of characteristics ranging from elastomeric, viscoelastic, to high-strength rigid.[7–13] As a result, there has been of great interest to develop novel DIW AM techniques to utilize custom feedstocks with tuned mechanical characteristics in more application spaces.[14–24]

The ability to 3D print parts onto unstructured surfaces unachievable with conventional DIW 3D printing methods has received much recent attention. Unstructured surfaces can be defined as those with uneven topographies in unconventional orientations such as upside-down or tilted, etc. In addition, an emerging application that extends AM capabilities is to fabricate new components directly onto existing structures, which could be used for appending new reinforcements, functional devices, or repair. However, conventional extrusion-based AM is restricted to layer-by-layer deposition in the XY plane on an even surface by a downward-facing extrusion nozzle. While previous work has explored appending new structures to existing structures in unconventional surfaces, it was still restricted to planar motion.[25] Nevertheless, many build surfaces may be highly

C. D. Armstrong, S. M. Montgomery, L. Yue, H. J. Qi
The George W. Woodruff School of Mechanical Engineering
Georgia Institute of Technology
Atlanta, GA 30332, USA
E-mail: qih@me.gatech.edu

The ORCID identification number(s) for the author(s) of this article can be found under https://doi.org/10.1002/aisy.202300516.

DOI: 10.1002/aisy.202300516

C. D. Armstrong, H. J. Qi
Renewable Bioproducts Institute
Georgia Institute of Technology
Atlanta, GA 30332, USA

F. Demoly
ICB UMR 6303 CNRS
Belfort-Montbeliard University of Technology
UTBM
Belfort 90010, France

K. Zhou
Singapore Centre for 3D Printing
School of Mechanical and Aerospace Engineering
Nanyang Technological University
50 Nanyang Avenue, Singapore 639798, Singapore

nonplanar. To address this, conformal extrusion-based 3D printing, deposition of nonplanar layers, techniques have been developed by customized control algorithms as well as use of multiaxis robotic arms to modify motion of the build plate and/or extrusion head in 3D.[26–32] It is noted that an important aspect of conformal printing is to maintain the print nozzle to be perpendicular to the print substrate, which could allow better material deposition, especially when the substrate is highly slanted (such as near vertical). Previous control approaches have defined toolpath motion based on projections onto a print substrate model.[33] While this results in accurate traversal instructions, it is difficult to use printing more complex structures. Moreover, Alkadi et al. used Möller–Trumbore triangle–triangle intersection between stereolithography (STL) files to define conformal motion.[34] Yet, these approaches do not factor in surface normal direction of the print substrate model, thereby limiting conformal motion upon highly unstructured surfaces (such as highly slanted surface discussed earlier). Furthermore, while previous studies have successfully created geometries unattainable with conventional AM through dynamic reorientation of the extrusion nozzle, they move the build plate, which limits the size of existing structures and is unsuitable for fabricating structures onto an existing, fixed surface.[32,35,36] In addition, studies utilizing multiaxis rotation of the extrusion head predominantly used FFF to deposit rapidly solidifying thermoplastics rather than DIW.[37] This is because DIW AM outside of the downward XY plane presents a unique challenge: viscoelastic, shear thinning DIW inks are particularly sensitive to gravitational effects which can cause premature delamination of the structure from the print surface. As a result, conformal DIW techniques have been limited to 3D motion of a downward-facing extrusion nozzle, thereby limiting surfaces which the nozzle can travel without colliding with uneven features, such as the extremes of a cylinder.[38] Recently, researchers have overcome the gravitational constraint using rapidly solidifying DIW ink consisting of polymer networks catalyzed via ultraviolet (UV) irradiation.[25,39] Furthermore, depositing structures on inverted and horizontal surfaces has been accomplished through reorienting the extrusion nozzle; however, this technique is still restricted to planar layer deposition.[25] De Marzi et al. combined multiaxis rotation of the extrusion nozzle and use of rapidly polymerizing photopolymers subjected to continuous UV irradiation to successfully create a DIW technique theoretically capable of printing on highly unstructured surfaces; however, it has only been applied for printing freestanding lattices on planar surfaces.[40]

In this work, we introduce a conformal DIW manufacturing technique that utilizes a six-axis robotic arm and custom slicing algorithm to enable fabrication of structures on existing unstructured surfaces in any orientation (**Figure 1**a). We develop an algorithm that generates the print paths based on the calculated interaction points between the substrate and the print structure model. To ensure the extruded ink has good contact with the substrate, this algorithm also always positions the printing nozzle in the normal direction of the surface (Figure 1b). We employ a variety of materials including rapidly solidifying photopolymers, hydrophobic fumed silica, and high-strength dual network thermoset polymers for different potential applications. We demonstrate printing structures on fixed convex and concave cylindrical surfaces, appending support to a bracket, and the structural repair to restore the damaged features of an ancient sculpture based on a 3D scan. Moreover, we further demonstrate the ability to print on existing structures by depositing conductive paths on the surface of a printed support structure to enable deformation and load sensing functionality. Our technique enables fabrication on geometries previously unachievable using DIW 3D printing. This allows for a myriad of material feedstocks to be deposited directly onto end use substrates to suit many applications including structural repair, reinforcement, structural health monitoring, or restoration.

2. Experimental Section

2.1. DIW Ink Preparation

This work used four DIW inks for application-specific purposes. Ink 1 consisted of 92.2 wt% acrylate monomer blend, 0.8 wt% photo initiator Irgacure 819 (Bis(2,4,6-trimethylbenzoyl)-phenylphosphineoxide) (Sigma-Aldrich, St. Louis, MO, USA), and 7 wt% fumed silica (Sigma-Aldrich). The acrylate monomer blend consisted of 79 wt% isobornyl acrylate (IBOA), 19 wt% poly(ethylene glycol) diacrylate (PEGDA), and 2 wt% isodecyl acrylate (IDA) (Sigma-Aldrich). This blend of rigid (IBOA), cross-linking (PEGDA), and elastomeric (IDA) monomers yielded a strong, tough, and rapidly solidifying material. The monomer blend was hand mixed, then the photo initiator was added, followed by 10 min of magnetic stirring to homogenize the mixture.

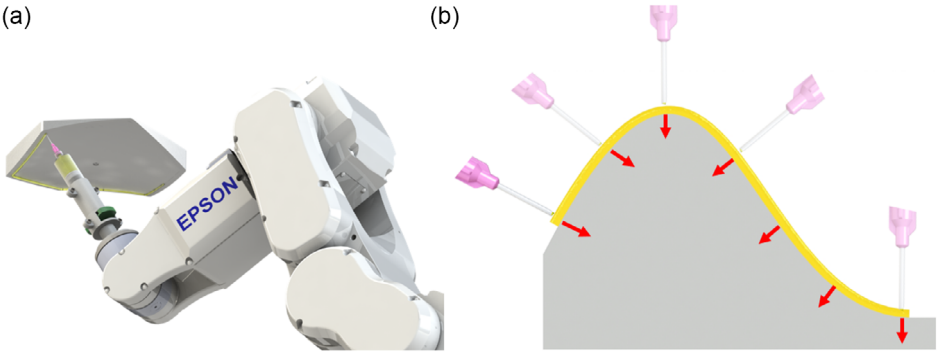

Figure 1. Graphical depiction of the multiaxis conformal DIW AM process, from algorithm to print. a) The DIW-fabricated nonplanar ring structure. b) Motion of the extrusion nozzle when depositing material following a curved substrate (represented in yellow).

Finally, fumed silica was mixed into the liquid resin to facilitate thixotropic behavior necessary for DIW 3D printing.

Ink 2 consisted of 85.2 wt% of the aforementioned monomer blend, 0.8 wt% photoinitiator, 14 wt% surface-modified hydrophobic fumed silica (Sigma-Aldrich), and was prepared in the same fashion. The addition of surface-modified hydrophobic fumed silica enabled printed structures to remain geometrically stable during prolonged contact with water by inhibiting water molecule interaction with the material, thereby reducing hydrolyzing degradation.

Ink 3 was a two-stage ambient curing resin consisting of photopolymer and epoxy resin components at a ratio of 30:70 wt%.[25] The monomers for the photopolymer resin component consisted of 95 wt% ethoxylated trimethylolpropane triacrylate (TMPTA) monomer (Sigma-Aldrich, St. Louis, MO, USA) and 5 wt% glycidyl methacrylate (GMA) (Sigma-Aldrich) as a reactive diluent. The monomers for the epoxy resin contained a 100:32 ratio of Epon 828 (difunctional bisphenol A/epichlorohydrin (DGEBA); Hexion, Columbus, OH, USA) and Jeffamine D230 curing agent (O,O′-Bis(2-aminopropyl) polypropylene glycol-block-polyethylene glycol-blockpolypropylene glycol) (Sigma-Aldrich). 1 wt% photo initiator Irgacure 819 (Sigma-Aldrich) and 3 wt% cocuring agent were added to the two-stage resin mixture to facilitate photopolymerization and catalyze room-temperature curing, respectively. The cocuring agent consisted of 70 wt% triethanolamine, 20 wt% piperazine, and 10 wt% *N*-aminoethylpiperazine (Sigma-Aldrich). 7 wt% fumed silica (Sigma-Aldrich) was mixed into the liquid two-stage resin.

Finally, a conductive ink was created using ME603 conductor paste (DuPont, Wilmington, DE, USA) mixed with 3 wt% Timical Super C45 carbon black (MTI Corporation, Richmond, CA, USA). The addition of carbon blacks was demonstrated to improve conductivity and improve shear-thinning behavior of the conductive ink.[41]

Once prepared, the DIW inks were loaded into syringes and centrifuged for 20 min to completely remove air bubbles and then mounted to an Epson C4 6-axis robotic arm (Epson, Suwa, Nagano, Japan).[42] DIW material deposition was achieved using compressed air delivered by an Ultimus V air-pressure controller (Nordson EFD, East Providence, RI, USA) to extrude the ink through an affixed deposition nozzle.

2.2. Algorithm for Printing Path

Conventional DIW printing occurred in the XY plane with the extrusion nozzle perpendicular to the flat substrate, which enabled good adhesion between layers. For our robotic conformal printing, we imposed this same requirement so that the extrusion tip dynamically reoriented itself to remain consistently perpendicular to the substrate during printing (Figure 1b). We developed a slicing algorithm that generated the print paths based on the calculated interaction points between the substrate and the print structure model. Each intersection point consisted of position $\{x, y, z\}$ and rotation angle $\{\alpha, \beta, \gamma\}$ information. The rotation angles were obtained via extrinsic Euler angle transformations that rotated the nozzle from its initial vertical orientation to the normal vector direction of the substrate model. Importantly, as the rotation angles were based upon the normal vectors of the print substrate model, the algorithm could generate toolpath information for material deposition in unconventional orientations such as inverted and vertical. The algorithm procedure is detailed in **Figure 2** and consists of five steps: 1) positioning substrate and print structure models; 2) establishing intersection points; 3) calculating normal vectors and obtaining rotation angles; 4) creating subsequent print layers based on topography offset; and 5) generating toolpath code for the multiaxis robotic arm (**Figure 3**a). The subsections below describe these steps.

2.2.1. Positioning of Substrate and Print Structure Models

The unstructured surface was a 3D model where the features were represented as vertices that define triangular faces. The structure to be printed was also defined in such a way. Using the 3D modeling program Blender (Amsterdam, NL), the 3D structure model to be printed was positioned on the surface in the desired print location. Next, the substrate surface and structure models were exported as separate STL files, where both models used robotic arm's coordinate system whose origin was placed at its base (Figure 3b). The STL files, which consisted of a set of triangular faces defined by their edges and faces, were then imported into a custom MATLAB script (MathWorks, Natick, MA, USA) where multiaxis slicing occurred.

2.2.2. Establishing Intersection Points

The MATLAB script utilizes a surface intersection function to determine x, y, and z coordinates of points at which the model and the substrate surface intersect.[43] The function applies the Möller–Trumbore triangle–triangle intersection algorithm to determine the points at which the surfaces intersect[44] (Figure 3c). The calculated intersection points define the positional component of the final print toolpath. In this regard, the density of triangular faces forming the print surface STL is directly proportional to the resolution of intersection points comprising the print toolpath, and greater triangular face density will result in improved rotation angle fidelity. However, in practice, a balance must be struck between STL surface resolution versus computational cost. Therefore, face resolution may need to be tuned during the generation of STL files by altering the mesh density of the original 3D model.

2.2.3. Assigning Normal Vectors and Obtaining Rotation Angles

The next step was to obtain the rotation angles (α, β, γ) of the extrusion nozzle such that it remains perpendicular to the substrate at each intersection point. This was accomplished by assigning a vertex normal vector, which was calculated as the average of the normal vectors of all the faces that share the vertex (Figure 3d). We then calculated a rotation matrix that rotates from the initial direction of the robotic arm $\mathbf{k} = \{0\ 0\ 1\}$ (vertical direction where the robot arm has zero rotations) to the vertex normal vector direction using the MATLAB functions *vrrotvec2mat*. The Euler angles were then extracted from the obtained rotation matrix using the function *rotm2eul* from the MATLAB Robotics System Toolbox. These angles were paired with the

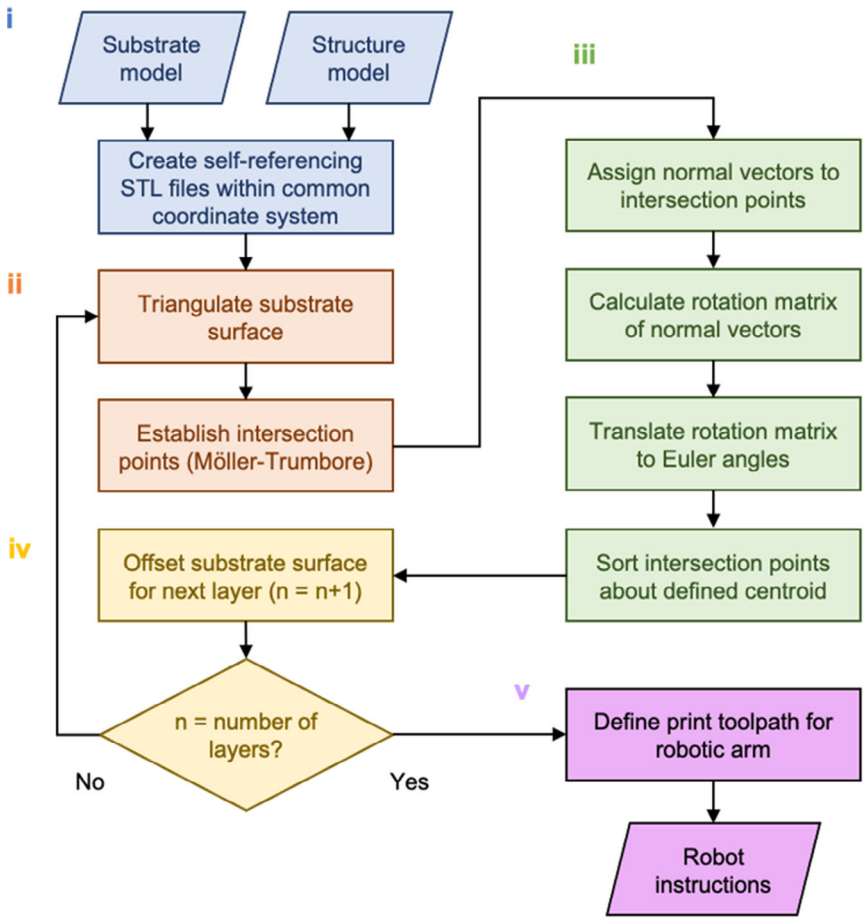

Figure 2. Flowchart outlining the process of creating a perpendicular conformal toolpath on an unstructured substrate.

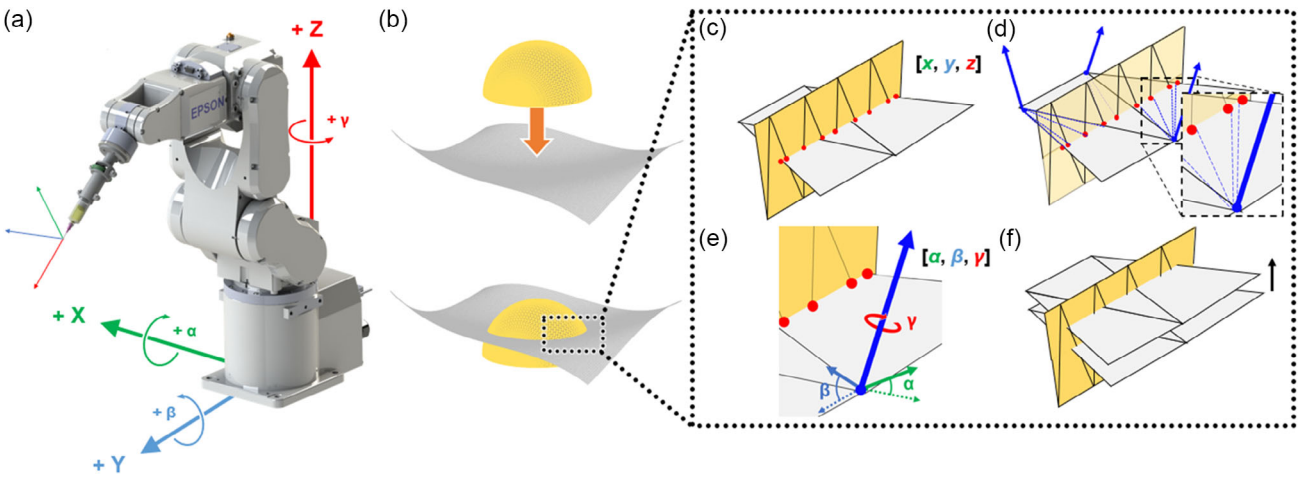

Figure 3. Graphical depiction of the slicing procedure. a) The robotic arm depicting the global and tool coordinate systems. b) Defining position of the triangulated model to be printed (yellow) with respect to the substrate surface model (gray). c) Calculating spatial intersection points $\{x, y, z\}$ (red) between the structure to be printed (yellow) and substrate (gray) using triangle–triangle intersection. d) Assigning normal vectors (blue) of substrate faces to intersection points based on proximity. e) Obtaining rotation angles $\{\alpha, \beta, \gamma\}$ from substrate normal vectors. f) Generating subsequent layers $n+1$ based on surfaces offset from the original substrate $n=0$.

point's spatial coordinates to create a spatial-rotation point $\{x, y, z, \alpha, \beta, \gamma\}$ that could be interpreted by the robot arm (Figure 3e).

The rotation angle (Figure 3e), which defines nozzle rotation about the z axis, can exhibit undesirable singularity in the tool path. As a result, it is necessary to define γ as a static value. To achieve this, we calculated an equivalent rotation matrix defined with $\gamma = 0$ for each normal vector. A root finding operation obtains the angles α and β that give the same final orientation as the original rotation matrix (R). The minimization function is defined as

$$\min f(\alpha, \beta) = 1 - ((\mathbf{R}(\alpha, \beta))\mathbf{k} \cdot \mathbf{n}) \quad (1)$$

where $\mathbf{n}$ is the desired nozzle orientation, and $\mathbf{R}(\alpha, \beta)$ is the new rotation vector with $\gamma = 0$. R is calculated using the internal MATLAB function *eul2rotm* from the Robotics System Toolbox. Equation (1) was minimized when the dot product between the desired nozzle orientation and the nozzle orientation achieved using the new equivalent rotation matrix was equal to 1.

2.2.4. Creating Subsequent Print Layers Based on Topography Offset

DIW is a layer-by-layer fabrication process; therefore, the model to be printed must be sliced into discretely stacked layers. In our algorithm, once all the position–normal points where the model to be printed intersects with the original substrate were calculated, a new triangulated surface was created by a specified layer height distance above the original substrate (Figure 3f). In order to reflect spatial changes of the surface topography relative to the distance from the original substrate, a surface offset function was used.[45] The subsequent layer surface was created by referencing the faces and vertices comprising the original substrate surface and projecting them outward along the substrate face normal direction at the desired layer thickness multiplied by the current layer number. Because the model to be printed remains fixed relative to the substrate model (Section 2.2.1), the intersections between this new surface and the model to be printed define the toolpath movement for a layer to be extruded upon the previous layer; thus enabling layer-by-layer deposition required for DIW 3D printing. Position–rotation points were calculated on this layer repeating the methodologies described in Section 2.2.2 and 2.2.3.

2.2.5. Generating Toolpath Code for the Multiaxis Robotic Arm

Finally, once the specified layer count was reached, print toolpaths were generated in the Epson SPEL+ machine language. An individual point was defined in terms of calculated $\{x, y, z, \alpha, \beta, \gamma\}$ values, which the robotic arm was instructed to move in a continuous path to the next defined point in the toolpath. Furthermore, pauses where the nozzle was moved away from the print structure were inserted every three layers so that the structure can be exposed to UV irradiation in order to solidify the photopolymerizable feedstock.

2.3. Creation and Preparation of Unstructured Substrates

Unstructured substrates in this work were fabricated using an Ender-5 FFF printer (Creality, Shenzhen, China). These substrates were developed through either a computer-aided design (CAD) software, or from 3D scans of an existing object. The created substrate models were imported into the slicing software Repetier Host (Hot-World GmbH & Co. KG, Willich, Germany) to produce G-code toolpath instructions for the FFF printer.

2.4. 3D Printing of Structures

Models were prepared using SolidWorks or acquired via Thingiverse.com (under public domain license). Prior to printing, the models were sliced into discrete layers consisting of point-rotation coordinate toolpaths using the algorithm discussed in Section 2.2. Structures were subsequently printed using a 20 gauge ($d = 0.58$ mm) nozzle at a speed of 10 mm s^{-1}. UV irradiation (66 mW cm^{-2}) was applied for five seconds (or 15 s in the case of two-stage curing ink) every third layer. To integrate functional elements, the syringe containing polymer ink was exchanged for one containing conductive ink and were deposited following a separately defined toolpath.

3. Results and Discussion

3.1. Multidimensional 3D Printing

To demonstrate the diversity of substrates and print orientations our robotic conformal printing technique is capable of, we 3D print on cylindrical substrates using ink 1 (**Figure 4**a–c and Video S1, Supporting Information). The cylindrical substrate models are created using SolidWorks CAD software. Using the dynamically reconfigurable α, β, γ nozzle orientation, the technique enables printing on the entire top face (0–π) of a static cylinder (Figure 4a–c). Depositing material at the extreme ends (0 and π angles) of the cylindrical face is unachievable using conventional DIW or previous conformal printing techniques with fixed nozzle orientation because the nozzle would eventually collide with or overshoot the surface. This issue is overcome by our technique of dynamically reorienting the nozzle to be always perpendicular to the substrate surface. Additionally, this technique is capable of printing on inverted cylindrical substrates, as shown in Figure 4d, where ink 2 is being used to patch over a hole ($d = 10$ mm). These experiments indicate that our printing approach has potential applications in on-site repair of structures which cannot or are too cumbersome to move. For example, the dynamically oriented nozzle motion coupled with the material versatility characteristic of DIW can be used to mend pipes. Indeed, the rapidly solidifying, hydrophobic nature of ink 2 used to mend the hole in Figure 4d is highly appropriate for repair of water transportation infrastructure. Similar photopolymerizable resins have been shown to exhibit strong surface adhesion to a variety of substrates, including acrylic, glass, aluminum, wood, and concrete.[25] Further work is required to determine the stability of such a patch in the context of a fluid-carrying pipe. Moreover, the dexterity of the multiaxis robotic arm platform introduces the possibility of repairing internals of structures provided there is

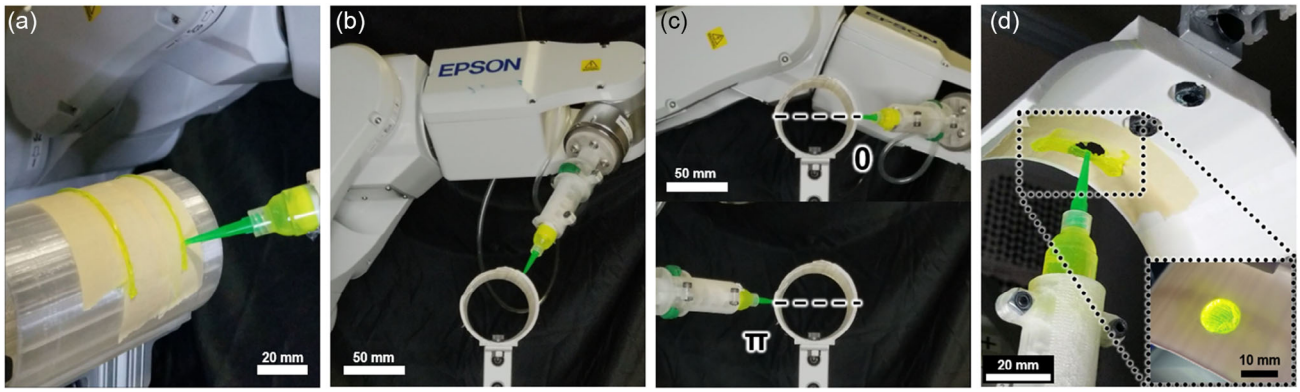

Figure 4. 3D printing onto cylindrical surfaces. a) Depositing layers on top of the cylinder. b) The robotic arm traversing the cylindrical surface as viewer from the front. c) Extrusion nozzle positioned at the extremes of the semicircular path. d) Inverted printing of a hydrophobic patch over a hole ($d = 10$ mm) on a curved substrate.

sufficient space for arm joints. This capability would enable repair in spaces too tight or too unstable for safe human intervention.

3.2. 3D Printing of Structural Reinforcement with Health Monitoring

Another use case of multiaxis robotic conformal printing is presented in **Figure 5**a, wherein an inverted "L"-shaped bracket is mechanically reinforced with a printed diagonal structure bridging the perpendicular surfaces. Such a path is not traversable with a fixed extrusion nozzle angle, the bracket would need to be rotated 45° to fabricate a comparable structure. Here, we use ink 3, which is a dual-polymer network and is ideal for this application as it develops a high strength with exceptional adhesion to a wide variety of substrates after curing for 72 h in ambient temperature conditions.[25] To exhibit the effectiveness of the high-strength printed reinforcement, identical brackets with and without reinforcement are subjected to

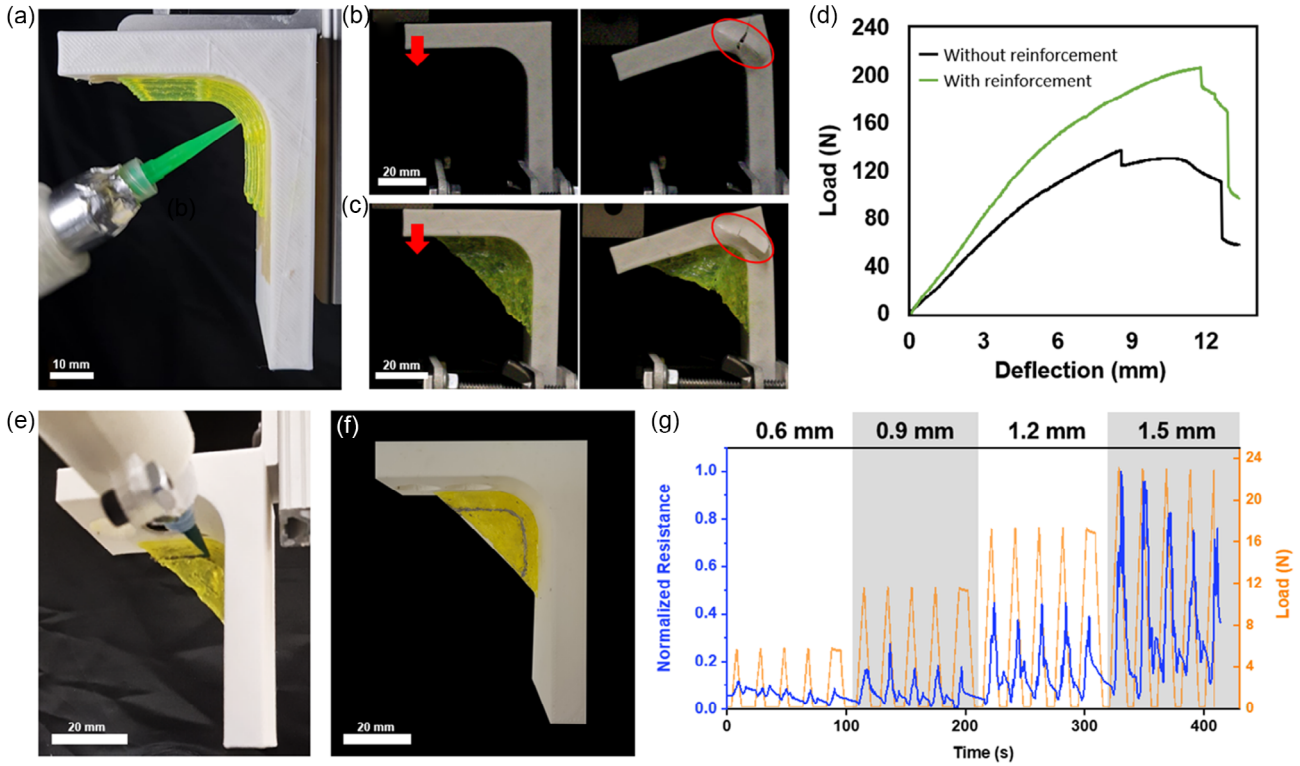

Figure 5. Multidimensional fabrication on an inverted "L"-shaped right-angle bracket. a) Fabricating a high-strength reinforcement on the bracket. b) Mechanical loading on an unreinforced bracket $t = 0$ (left), moment of failure (right). c) Mechanical loading on a bracket with printed reinforcement $t = 0$ (left), moment of failure (right). d) Graph depicting load versus deflection behavior of the reinforced and unreinforced brackets. e) Depositing a conductive path onto the surface of the printed reinforcement. f) A functional structure for sensing deflection of the bracket with respect to load. g) Normalized resistance (blue) and force (orange) responses to 0.6, 0.9, 1.2, and 1.5 mm deflections over time.

compressive loading (Figure 5b,c). Load–deflection plots are presented in Figure 5d, and experiments are recorded in Video S2, Supporting Information. Addition of printed reinforcement affords a 50% increase in both maximum load at yield and load at failure over the unreinforced bracket (206.69 vs 137.70 N and 169.18 vs 110.76 N, respectively). Furthermore, the reinforced bracket shows a 34% increase in stiffness over the unreinforced bracket (26.77 vs 19.99 N mm^{-1}).

Additionally, we deposit conductive ink paths on the surface of the diagonal support to create a functional 3D-printed structure capable of in situ deformation sensing (Figure 5e,f, Video S3, Supporting Information). To achieve deposition without moving the existing structure, the multiaxis robotic arm reorients the nozzle extrusion angle perpendicular to the reinforcement (Figure 5e). The results of normalized resistance and loading over time for the sensor subjected to cyclic deflection five times at $\delta = 0.6$, and 0.9, 1.2, and 1.5 mm are presented in Figure 5g. The increasing magnitude deflection cycles are performed in a continuous experiment. The plotted resistance shows peaks of increasing amplitude in the sensor signal corresponding to prescribed deformation. Additionally, the peaks coincide with increasing force exerted on the bracket, thereby demonstrating the printed sensor's potential to represent not only mechanical deformations but also force magnitudes in the structure. Based on these trends, this functional printed reinforcement has the ability to monitor deformations and loads in a pre-existing structure in situ, which could be invaluable in structural health-monitoring applications.

3.3. Restoration and Repair

As discussed in the previous section, this multiaxis conformal printing technique is a highly capable method of on-site surface repair. Additionally, this technique can also be applied for restoration of a "real-world" structure by printing complex customized 3D features onto substrates derived from 3D scans. 3D scan resolution is an important factor in generating a high-quality STL model. The importance of triangular face is discussed in Section 2.2.2. We demonstrate this using the famous example of restoring the nose to a defaced Ancient Egyptian sculpture (**Figure 6**a, Video S4, Supporting Information). The 3D scan was originally obtained using Autodesk 123D Catch, and the 3D model used was obtained from the Thingiverse online platform. We then position our own 3D model of a nose onto the derived 3D model of the substrate (Figure 6b). Using the slicing algorithm detailed in Section 2, a high-resolution ($n = 60$ layers) toolpath of points $\{x, y, z, \alpha, \beta, \gamma\}$ model is generated relative to the triangulated surface (Figure 6c,d). It is important to note the nonplanar contoured nature of the toolpath layers, which are indicative of the extrusion nozzle tracing about fractured bridge of the nose. This topographical region extends awkwardly outward due to the highly unstructured, semirandom nature of

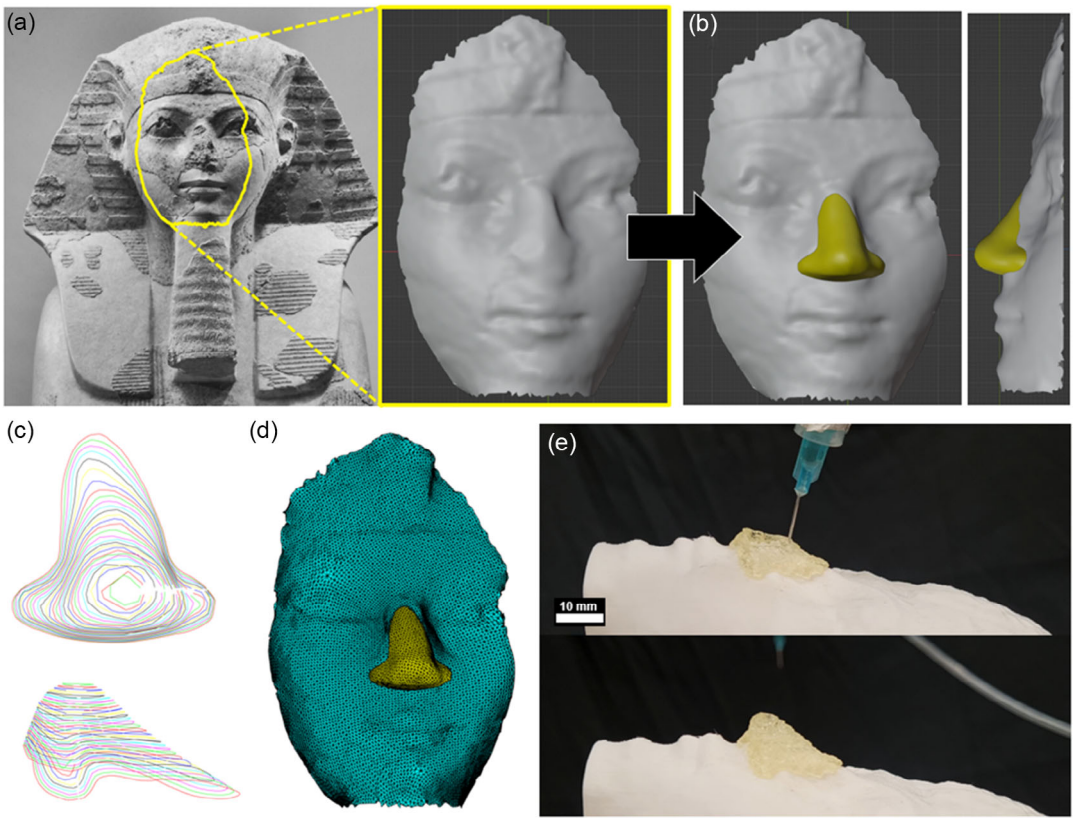

Figure 6. Process of conformal printing a "real-world" substrate. a) The original damaged bust. b) A 3D scan of the face of the bust with nose model to be printed positioned in the appropriate place. c) Toolpaths of layers ($n = 60$). d) Triangulated face substrate with nose as seen in the slicing process. e) Printing of the nose structure on an FFF-built substrate based on the original 3D scan.

the desired repair area caused by the blunt strike which defaces the sculpture. Thus, the ability to tilt the axis of deposition is vital to traversing about such features which may otherwise impede or collide with a vertically oriented extrusion nozzle. Finally, the created 3D restoration is printed onto a replica of the face using ink 1, which is advantageous in the event the sculpture cannot be laid flat due to gravitational effects (Figure 6e). DIW is an ideal technique for this use case as a feedstock material may be modified with ceramic particles or dyes in order to better replicate the original material in feel and appearance.[46]

4. Conclusions

In this work, we developed a multiaxis robotic conformal DIW printing technique, facilitated by a custom slicing algorithm, capable of dynamically orienting extrusion head to be continuously perpendicular to the substrate. This manufacturing technique enables fabrication of complex structures on fixed unstructured surfaces previously unachievable with conventional manufacturing or 3D printing techniques, including unconventional orientations such as inverted, and horizontal, rough or complex topographies, and multiplanar substrates. Moreover, the use of DIW 3D printing allows for a vast breadth of material compositions to be utilized, including rapidly polymerizing thermosets, hydrophobic materials, and tough dual-network epoxy resins directly onto end use substrates to suit many applications including structural repair, reinforcement, or restoration. The demonstrations suggest this technique could potentially be applied for rapid, automated, and precise on-site repair in human-limited areas which have spatial constraints or environmental hazards. Furthermore, incorporation of conductive elements to a high-strength structural reinforcement allows for creation of functional structures capable of in situ deflection monitoring through a single-stream process.

Supporting Information

Supporting Information is available from the Wiley Online Library or from the author.

Acknowledgements

H.J.Q. acknowledges the support of AFOSR grants (FA9550- 19-1-0151 and FA9550-20-1-0306; Dr. B.-L. "Les" Lee, Program Manager). H.J.Q. also acknowledges the gift funds from HP, Inc.

Conflict of Interest

The authors declare no conflict of interest.

Data Availability Statement

The data that support the findings of this study are available from the corresponding author upon reasonable request.

Keywords

3D printing, additive manufacturing, functional structures, robotic printing

Received: August 27, 2023
Revised: November 7, 2023
Published online: January 9, 2024

[1] M. A. H. Khondoker, N. Baheri, D. Sameoto, *3D Print. Addit. Manuf.* **2019**, *6*, 191.
[2] C. D. Armstrong, N. Todd, A. T. Alsharhan, D. I. Bigio, R. D. Sochol, *Adv. Mater. Technol.* **2021**, *6*, 2000829.
[3] M. Lanaro, D. P. Forrestal, S. Scheurer, D. J. Slinger, S. Liao, S. K. Powell, M. A. Woodruff, *J. Food Eng.* **2017**, *215*, 13.
[4] R. Matsuzaki, M. Ueda, M. Namiki, T.-K. Jeong, H. Asahara, K. Horiguchi, T. Nakamura, A. Todoroki, Y. Hirano, *Sci. Rep.* **2016**, *6*, 23058.
[5] X. R. Peng, X. Kuang, D. J. Roach, Y. Wang, C. M. Hamel, C. Lu, H. Jerry Qi, *Addit. Manuf.* **2021**, *40*, 101911.
[6] A. Gleadall, *Addit. Manuf.* **2021**, *46*, 102109.
[7] C. D. Armstrong, L. Yue, Y. Deng, H. J. Qi, *J. Food Eng.* **2022**, *330*, 111086.
[8] V. C.-F. Li, C. K. Dunn, Z. Zhang, Y. Deng, H. J. Oi, *Sci. Rep.* **2017**, *7*, 8018.
[9] Q. Fu, E. Saiz, A. P. Tomsia, *Acta Biomater.* **2011**, *7*, 3547.
[10] B. Kim, B. Kim, A. H. Soepriatna, W. Park, H. Moon, A. Cox, J. Zhao, N. S. Gupta, C. H. Park, K. Kim, Y. Jeon, H. Jang, D. R. Kim, H. Lee, K.-S. Lee, C. J. Goergen, C. H. Lee, *Nat. Commun.* **2021**, *12*, 3710.
[11] D. J. Roach, C. Yuan, X. Kuang, V. C.-F. Li, P. Blake, M. L. Romero, I. Hammel, K. Yu, H. J. Qi, *ACS Appl. Mater. Interfaces* **2019**, *11*, 19514.
[12] V. G. Muir, T. H. Qazi, S. Weintraub, B. O. Torres Maldonado, P. E. Arratia, J. A. Burdick, *Small* **2022**, *18*, 2201115.
[13] X. R. Peng, S. Wu, X. Sun, L. Yue, S. M. Montgomery, F. Demoly, K. Zhou, R. R. Zhao, H. J. Qi, *Adv. Mater.* **2022**, *34*, 204890.
[14] L. Friedrich, M. Begley, *J. Colloid Interface Sci.* **2018**, *529*, 599.
[15] M. A. Skylar-Scott, J. Mueller, C. W. Visser, J. A. Lewis, *Nature* **2019**, *575*, 330.
[16] G. J. Cordonier, K. A. Sierros, *ACS Appl. Mater. Interfaces* **2020**, *12*, 15875.
[17] D. Tang, L. Hao, Y. Li, Z. Li, S. Dadbakhsh, *J. Alloys Compd.* **2020**, 814.
[18] S. Wu, C. M. Hamel, Q. Ze, F. Yang, H. J. Qi, R. Zhao, *Adv. Intell. Syst.* **2020**, 2000060.
[19] Y. Jiang, X. Wang, J. Plog, A. L. Yarin, Y. Pan, *J. Manuf. Processes* **2021**, *69*, 173.
[20] C. Zhou, Y. Yang, J. Wang, Q. Wu, Z. Gu, Y. Zhou, X. Liu, Y. Yang, H. Tang, Q. Ling, L. Wang, J. Zang, *Nat. Commun.* **2021**, *12*, 5072.
[21] C. Ma, S. Wu, Q. Ze, X. Kuang, R. Zhang, H. J. Qi, R. Zhao, *ACS Appl. Mater. Interfaces* **2021**, *13*, 12639.
[22] A. Charlet, F. Bono, E. Amstad, *Chem. Sci.* **2022**, *13*, 3082.
[23] C. Ma, Y. Chang, S. Wu, R. R. Zhao, *ACS Appl. Mater. Interfaces* **2022**, *14*, 33892.
[24] Q. Ze, S. Wu, J. Dai, S. Leanza, G. Ikeda, P. C. Yang, G. Iaccarino, R. R. Zhao, *Nat. Commun.* **2022**, *13*, 3118.
[25] C. D. Armstrong, L. Yue, F. Demoly, K. Zhou, J. Qi, *Adv. Intell. Syst.* **2022**, *5*, 2200226.
[26] F. B. Coulter, A. Ianakiev, *3D Print. Addit. Manuf.* **2015**, *2*, 140.
[27] C. Dai, C. C. L. Wang, C. Wu, S. Lefebvre, G. Fang, Y.-J. Liu, *ACM Trans. Graphics* **2018**, *37*, 134.
[28] J. R. Kubalak, A. L. Wicks, C. B. Williams, *Rapid Prototyping J.* **2019**, *25*, 356.

[29] E. Gunpinar, S. Cam, *Graphical Models* **2022**, *120*, 101137.
[30] E. Gunpinar, A. Armanfar, *J. Mater. Process. Technol.* **2022**, *304*, 117565.
[31] N. R. Fry, R. C. Richardson, J. H. Boyle, *Rapid Prototyping J.* **2020**, *26*, 659.
[32] B. J. Brooks, K. M. Arif, S. Dirven, J. Potgieter, *Int. J. Adv. Manuf. Technol.* **2017**, *89*, 957.
[33] C. Rodriguez-Padilla, E. Cuan-Urquizo, A. Roman-Flores, J. L. Gordillo, C. Vázquez-Hurtado, *Appl. Sci.* **2021**, *11*, 7509.
[34] F. Alkadi, K.-C. Lee, A. H. Bashiri, J.-W. Choi, *Addit. Manuf.* **2020**, *32*, 100975.
[35] J. Huang, H. O. T. Ware, R. Hai, G. Shao, C. Sun, *Adv. Mater.* **2021**, *33*, 2005672.
[36] J. J. Adams, E. B. Duoss, T. F. Malkowski, M. J. Motala, B. Y. Ahn, R. G. Nuzzo, J. T. Bernhard, J. A. Lewis, *Adv. Mater.* **2011**, *23*, 1335.
[37] X. Song, Y. Pan, Y. Chen, *J. Manuf. Sci. Eng.* **2015**, *137*, 021005.
[38] J. L. Pérez-Castillo, E. Cuan-Urquizo, A. Roman-Flores, O. Olvera-Silva, V. Romero-Muñoz, A. Gómez-Espinosa, R. Ahmad, *Addit. Manuf.* **2021**, *47*, 102354.
[39] T. Wu, P. Jiang, X. Zhang, Y. Guo, Z. Ji, X. Jia, X. Wang, F. Zhou, W. Liu, *Mater. Des.* **2019**, 180107947.
[40] A. De Marzi, M. Vibrante, M. Bottin, G. Franchin, *Addit. Manuf.* **2023**, *66*, 103456.
[41] C. D. Armstrong, L. Yue, X. Kuang, D. J. Roach, M. L. Dunn, J. Qi, *J. Compos. Mater.* **2022**, *57*, 841.
[42] D. J. Roach, C. M. Hamel, C. K. Dunn, M. V. Johnson, X. Kuang, H. J. Qi, *Add. Manuf.* **2019**, *29*, 100819.
[43] J. Tuszynski, MATLAB Central File Exchange **2023**.
[44] T. Möller, B. Trumbore, in *SIGGRAPH '05: ACM SIGGRAPH 2005 Courses*, ACM Press, New York **2005**, https://doi.org/10.1145/1198555.1198746.
[45] K. Moerman, MATLAB Central File Exchange **2023**.
[46] J. A. Lewis, *J. Am. Ceram. Soc.* **2000**, *83*, 2341.